# Detection Of Precipitation Using Scanning Radars With Strong Sectorial Interferences

Dash, Tworit; Lu, Wenyi; Krasnov, Oleg; Yarovoy, Alexander

**DOI**
10.1109/IGARSS53475.2024.10642725

**Publication date**
2024

**Document Version**
Final published version

**Published in**
Proceedings of the IGARSS 2024 - 2024 IEEE International Geoscience and Remote Sensing Symposium

**Citation (APA)**
Dash, T., Lu, W., Krasnov, O., & Yarovoy, A. (2024). Detection Of Precipitation Using Scanning Radars With Strong Sectorial Interferences. In *Proceedings of the IGARSS 2024 - 2024 IEEE International Geoscience and Remote Sensing Symposium* (pp. 515-519). IEEE. https://doi.org/10.1109/IGARSS53475.2024.10642725

IGARSS 2024 - 2024 IEEE International Geoscience and Remote Sensing Symposium | 979-8-3503-6032-5/24/$31.00 ©2024 IEEE | DOI: 10.1109/IGARSS53475.2024.10642725

# DETECTION OF PRECIPITATION USING SCANNING RADARS WITH STRONG SECTORIAL INTERFERENCES

*Tworit Dash**
Delft University of Technology
Microelectronics
Mekelweg 4, Delft

*Wenyi Lu*
TU Delft
Microelectronics
Mekelweg 4, Delft

*Oleg Krasnov*
TU Delft
Microelectronics
Mekelweg 4, Delft

*Alexander Yarovoy*
TU Delft
Microelectronics
Mekelweg 4, Delft

## ABSTRACT

The problem of precipitation detection using Frequency Modulated Continuous Wave (FMCW) radar under strong sectorial interference is addressed. The effect of such strong interferences in the case of an FMCW scanning radar is presented. Three signal-processing pipelines (two reflectivity-based and one Doppler-based) are proposed. The performances of all these pipelines are analyzed and compared. The morphology-based pipeline performs better for higher signal-to-noise ratios ($> -15$dB), whereas the entropy-based pipeline performs better in the case of lower SNRs ($< -15$dB). On the other hand, the circular variance-based masking technique is computationally very efficient. The proposed techniques are applied to simulated and real X-band fast-scanning radar data.

***Index Terms***— Sectorial Noise, Doppler spectrum, Entropy, Circular variance

## 1. INTRODUCTION

Modern FMCW fast azimuthal scanning radars deployed at airports are primarily used to detect and track point-like targets such as birds and drones [1]. Recently, there has been a growing demand to upgrade such radar systems to have the capability to detect precipitation-like targets and estimate the velocity of such targets. The knowledge of the spatial distribution of precipitation strength and their motion is essential for airplanes, especially during take-offs and landings.

Several challenges are associated with detecting precipitation targets with such radar systems. One such major challenge is the presence of strong interferences in some azimuthal sectors. Precipitation areas with lower reflectivities (total power received) can be easily hidden under these strong interferences. The cause of such interferences can be internal to the radar system hardware or external, such as strong reflecting targets like buildings. There are several techniques to address the detection of such interference-contaminated sectors.

The existing detection and classification of hydrometeors techniques rely on polarimetric observables such as differential reflectivity ($Z_{dr}$) and specific differential phase ($K_{dp}$). Although polarimetric retrievals are sensitive to the shape and size of hydrometeors, helping in classifying different hydrometeors (rain, snow, hail, etc), measuring such quantities poses additional calibration issues [2]. Image processing algorithms that use fuzzy logic suffer from computational issues, making them inefficient [3]. As we consider fast azimuthally scanning radar systems, it is adequate to use only one polarization but exploit the Doppler spectrum information to detect precipitation faster and more efficiently. The sectorial interferences (at several azimuthal directions) leave artifacts on the retrieved Doppler moments. In this paper, we discuss the effect of interference on the statistical Doppler spectrum moments.

This paper proposes three target masking techniques that can be used with single-polarized fast-scanning Doppler radar retrievals. The first is a morphology-based pipeline, the second is an entropy-based one, and the third is based on circular variance [4, Ch. 2]. The first two are reflectivity-based (zeroth moment of the Doppler spectrum), and the third is Doppler velocity-based.

The paper's main contributions are the use of information entropy of the radar retrieved reflectivity information to mask the radar targets other than precipitation and circular statistics to detect the weather targets contaminated with sectorial interferences. The morphology-based radar target masking technique is not new and has been discussed in the literature [5], [6]. However, we propose an application-specific modified morphology-based target masking pipeline that considers a step-by-step approach to eliminate targets other than precipitation.

## 2. EFFECT OF INTERFERENCE ON DOPPLER MOMENTS

Interference in specific azimuthal sectors intensifies reflectivity (the zeroth moment of the Doppler spectrum is the

*Thanks to "European Regional Development Fund (ERDF) via the Kansen voor West II Program" under the project "Airport Technology Lab." for funding this project.

total power these echo samples receive), notably higher than precipitation-like targets, exhibiting a saturated reflectivity with minimal variance along the range.

Interference also significantly impacts Doppler spectrum width (the square root of the second central Doppler moment; typically a measure of turbulence in the precipitation). The weather radars are usually designed such that the precipitation-like weather targets maintain a normalized spectral width below 0.1 (for a normalized Doppler velocity interval [-0.5, 0.5]) because estimators become biased above a normalized Doppler spectrum width of 0.2 [7]. Normalized Doppler spectrum width beyond 0.15 can be characterized as a "flat" spectrum. The spectrum is flat enough to conceal precipitation responses in the presence of interference.

A theoretical distinction between contaminated sectors and precipitation can be achieved based on reflectivity and spectral widths. Practical challenges arise with fast-scanning radars due to limited time per resolution volume. Insufficient Doppler resolution biases width estimates, especially when mean Doppler velocity (first Doppler moment) approaches the unambiguous velocity limit, causing spectrum folding/ aliasing. Advanced spectral width estimators like the parametric spectrum estimator [8] or complex Gaussian process method [7] address Doppler folding but can be computationally expensive. To overcome this, we propose using circular variance, which is immune to Doppler spectrum folding and computationally efficient (explained in section 3).

## 3. TARGET MASKING TECHNIQUES

This section presents three distinct masking techniques instead of a single combined approach to highlight their unique principles and functionalities. The reason for showcasing three separate techniques is that each method operates on different principles: morphology-based, entropy-based, and circular variance-based methods. Their performances and applicability are discussed in detail in section 4 through numerical simulations, emphasizing their diverse applications and advantages.

### 3.1. Morphology based target mask

The morphology-based target mask uses reflectivity information and has several steps, which are as follows. First, a cell-averaging constant false alarm rate (CA-CFAR) technique is used along ranges to detect high levels of reflectivity [9]. As discussed in the introduction, the interference-contaminated regions also have high levels of reflectivity. Still, the variance of reflectivity along the range is smaller than that of point targets, which is advantageous.

After the point target detection, the contaminated azimuthal directions are detected by assessing the mean reflectivity along the range for each azimuthal direction. A threshold can then be applied to remove the azimuthal sectors having larger mean reflectivity than the threshold. These azimuthal sectors are made void for further steps.

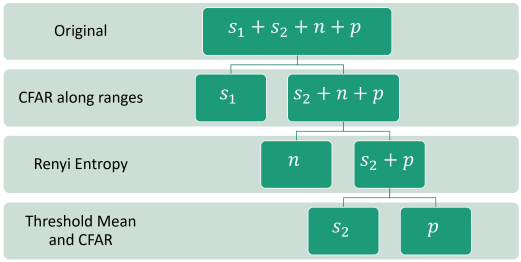


**Fig. 1**: Entropy-based pipeline

The wavelet-based denoising technique is used in the third step to reduce the noise from the reflectivity profile while still sufficiently retaining essential features of the targets [10]. A detailed analysis of the steps followed for denoising can be found in [11, Ch. 4.3.3].

After the denoising phase, morphological operations like erosion and dilation are performed further to refine specific features of interest within the reflectivity profile. A detailed step-by-step approach can be found in [11, Ch. 4.3.4]. Finally, the interference regions are filled by another morphological operation by selectively expanding and contracting target regions.

### 3.2. Entropy based target mask

For entropy-based masking, the reflectivity field $f(r, \phi)$ at a constant elevation angle $\theta$ is assumed to be a combination of four classes: point targets $s_1(r, \phi)$, precipitation $s_2(r, \phi)$, thermal noise $n(r, \phi)$, and interference $p(r, \phi)$ (where $r$ is the range, and $\phi$ is azimuthal angle).

$$f(r, \phi) = s_1(r, \phi) + s_2(r, \phi) + n(r, \phi) + p(r, \phi) \quad (1)$$

The steps followed in the entropy-based pipeline are shown in Fig. 1. The first step in the entropy-based pipeline is the same as the morphology-based pipeline. The second step involves using Rényi's entropy [12] to separate thermal global noise. The use of Rényi's entropy to create masks for targets was proposed in [13]. Rényi's entropy is used here to obtain a threshold between two sets of probability distributions. The two probability distributions are related to $n$ and $s_2 + p$, respectively. If the probabilities of the reflectivity values for $n$ and $s_2 + p$ are denoted as $p_A$, and $p_B$ and $H_\alpha^A$, and $H_\alpha^B$ represent their respective Rényi entropies with parameter $\alpha$ (which was set to $0.2$), the optimization problem to obtain the threshold is the following:

$$t(\alpha) = \underset{t}{\operatorname{argmax}} \left[ H_\alpha^A(t) + H_\alpha^B(t) \right], \quad (2)$$

where $H_\alpha^Q(t) = \frac{1}{1-\alpha} \log_2 \left( \sum_{i=1}^{t} (p_i / P_Q)^\alpha \right)$. The last step is to detect the interference, which is carried out by thresholding based on the mean reflectivity along the ranges and a

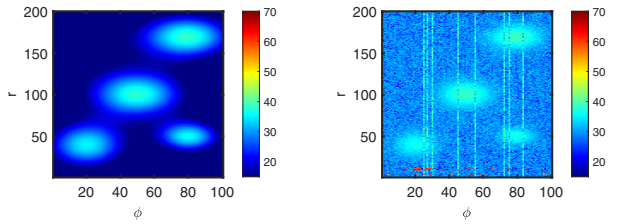


(a) (b)

**Fig. 2**: Simulation of targets; the x and y axes are indices in azimuth and range; the reflectivity data is in dB scale. (a) Precipitation only simulation (b) Simulation with precipitation, interference, thermal noise, and point targets.

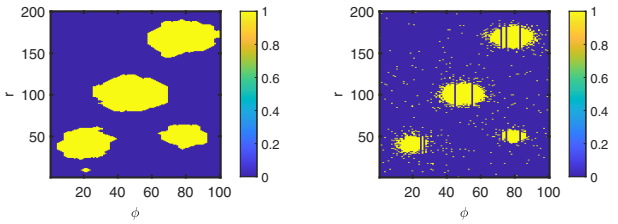


(a) (b)

**Fig. 3**: Target binary masks; 1 refers to precipitation and 0 refers to no-precipitation (a) Morphology based (b) Entropy based.

CA-CFAR to take the variance along the ranges into account. A detailed explanation of all the steps can be referred to from [11, Ch. 4.3.4].

### 3.3. Circular variance based target mask

The circular variance is a measure of normalized velocity dispersion like the normalized spectral width, and the values range from 0 to 1. Unlike the popular non-parametric Discrete Fourier Transform (DFT) based Doppler moment estimator [14], [15], the circular moment estimator uses a circular axis for the Doppler frequencies [4, Ch. 2], [11, Ch. 3, eq. 3.20]. Therefore, Doppler folding does not affect circular Doppler mean and variance estimation. The circular variance is studied with respect to the difference between the peak of the signal and the peak of the thermal noise floor (DPP) in the following section 4.

## 4. NUMERICAL SIMULATIONS

### 4.1. For morphology and entropy-based masks

A reflectivity field as a function of range and azimuth was simulated with Gaussian-shaped precipitation targets in 2D polar coordinates inspired from the field of view of an X-band scanning radar [1]. The addition of thermal noise is done by specifying an input SNR, the point targets are added at specific range-azimuth cells with very high reflectivities, and the interference is added at particular sectors in azimuth [11, Ch. 4.1].

An example simulation is shown in Fig. 2b, and the corresponding ground truth with only the precipitation targets is shown in Fig. 2a. The corresponding results with the morphology-based pipeline are shown in Fig. 3a, and the entropy-based pipeline is shown in Fig. 3b. It can be observed that the morphology-based mask takes care of the gaps at the interference-contaminated regions, whereas there is no such gap filling in the entropy-based mask. A reference binary mask is considered to assess the performance using a half-power ($-3$dB) elliptical contour on each target. The following metrics are chosen to assess further the performance of such masking techniques with respect to SNR. They are the intersection over union (IoU), false alarm probability ($p_{\text{fa}}$), the missed detection probability ($p_{\text{md}}$), and the F1Score [11, Ch. 4.3.7, eq. (4.6-4.10)]. It can be noticed that at high

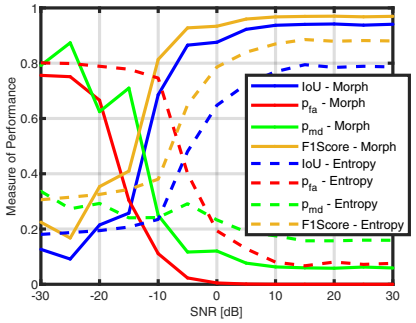


**Fig. 4**: Performace of morphology and entropy-based masking techniques. Solid lines are for morphology, and dotted ones are for entropy.

SNR regions ($> -15$dB), the morphology-based masking has higher IoU, lower false alarm rate, lower missed detections, and higher F1Score than the entropy-based one. On the other hand, for low SNR regions ($< -15$dB), the morphology-based masking technique has lower IoU, similar but more oscillating false alarm rate, higher missed detections, and lower F1Score than the entropy-based one. Therefore, it can be safely concluded that the morphology-based masking technique performs better at higher SNRs, and the entropy-based technique performs better at lower SNRs. Notably, the simulated targets have particular Gaussian shapes, and the structure elements used in the morphology-based masking are disk-shaped. For real-world radar observations, the precipitation targets are more diffused and do not have a particular shape. Therefore, these techniques are also applied to real-world radar data and are analyzed in the following section 5.

### 4.2. Detection criteria for circular variance-based mask

The circular variance is studied with respect to DPP and is shown in Fig. 5. A threshold of $0.8$ is set, and what are below $0.8$ are considered real precipitating targets. This technique depends on computations of the circular moments only over the Doppler spectrum, so it is computationally very efficient.

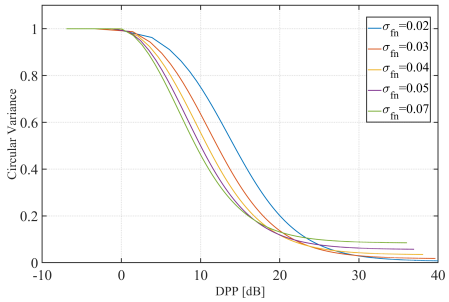


**Fig. 5**: Sensitivity of Circular Variance with DPP; $\sigma_{fn}$ is the normalized spectrum width.

## 5. APPLICATION TO REAL RADAR DATA

The X-band Max3D radar [1] was used to collect the real radar data; the specifications can be found in [16]. The plan position indicator (PPI) plots of the real radar data on a rainy day are presented in Fig. 6a at a zero-degree elevation, as much interference exists at this elevation. The corresponding masks are computed, and the original reflectivity values are multiplied by the masks. They are shown in Fig. 6b for morphology-based, Fig. 6c for entropy-based, and FIg. 6d for the circular variance-based masking techniques.

It can be observed that the morphology-based masking technique performs worse than the other two and only retains some information near the radar location. The algorithm's disk-shaped structure element assumption for precipitation-like targets is inadequate. The entropy-based and circular variance-based masking techniques perform similarly, and they both can, for example, detect the precipitation near $0°$ to $40°$ azimuth.

In the original reflectivity map, it can not be concluded about what is observed between $150°$, and $200°$ (clockwise) azimuth. Although the reflectivities are stronger than in the region from $0°$ to $40°$, they are not stronger than the interference regions, such as at around $45°$. The circular variance-based technique has masked this region of space, but the entropy-based technique still includes some parts. The lack of knowledge about the ground truth prohibits us from concluding which of these masking techniques performs better. On the contrary, in the region between $309°$ to $0°$ azimuth, much of the space is masked by the entropy-based masking pipeline, but some parts are still retained with the circular variance-based masking technique.

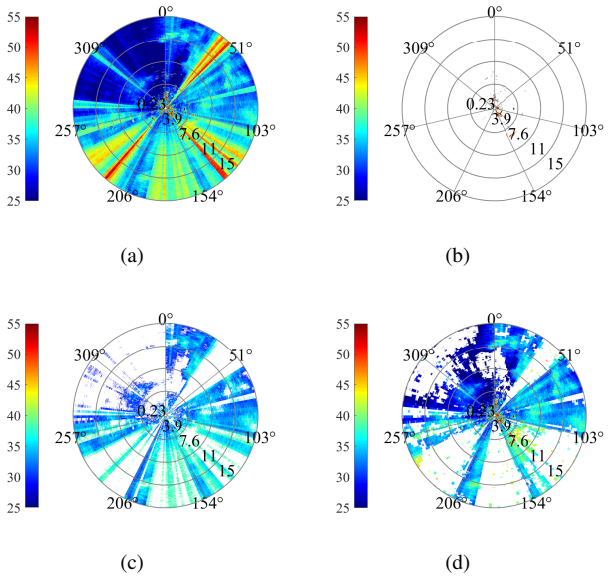


**Fig. 6**: Precipitation reflectivity maps, in dB, from real radar data (a) Original reflectivity, (b) Morphology-based detection, (b) Entropy-based detection, (d) Circular variance-based detection.

## 6. CONCLUSIONS

The effect of sectorial interferences on the Doppler spectrum moments is discussed, and based on that, three masking pipelines are proposed. The first two techniques are assessed using several metrics with simulated radar reflectivities. The third technique is based on the circular variance of the Doppler spectrum, and the importance of circular variance for masking is discussed, especially with folded Doppler spectra. On simulated reflectivity maps, the morphology-based pipeline performs better in the higher SNRs ($> -15$dB), and the entropy-based techniques perform better for lower SNRs ($< -15$dB). However, the morphology-based masking technique performs the worst on the real radar data by masking much of the observation region. This could be attributed to the assumption that the algorithm assumes a definite structure element for the precipitation-like targets (disk-shaped). The circular variance-based masking technique is computationally more efficient than the other two because it doesn't have many steps and only relies on the circular moment estimation of the Doppler spectrum. Both entropy and circular variance-based masking techniques perform similarly on the real radar data, except for some specific differences. The proposed pipelines are not compared with the existing polarimetry-based approaches in this paper, as we considered only the problem of precipitation detection (not classification) with sectorial noise. However, a detailed classification of extended weather targets (into rain, hail, snow, etc.) can be considered in the future with advanced entropy-based classification techniques.

## 7. REFERENCES


[1] "Robin Radar Systems full 3D Advanced Bird Detection Radar - MAX3D." [Online]. Available: https://www.robinradar.com/max-avian-radar-system

[2] C. Gatidis, M. Schleiss, and C. Unal, "Sensitivity analysis of DSD retrievals from polarimetric radar in stratiform rain based on the $\mu$-$\Lambda$ relationship," *Atmospheric Measurement Techniques*, vol. 15, no. 16, pp. 4951–4969, 2022.

[3] L. Pulvirenti, F. S. Marzano, N. Pierdicca, S. Mori, and M. Chini, "Discrimination of water surfaces, heavy rainfall, and wet snow using COSMO-SkyMed observations of severe weather events," *IEEE Transactions on Geoscience and Remote Sensing*, vol. 52, no. 2, pp. 858–869, 2014.

[4] K. V.Marida and P. E. Jupp, *Dirctional Statistics*, ser. Circular Data. John Wiley and Sons, Inc, 2000.

[5] S. S. Aung, I. Nagayama, and S. Tamaki, "An adaptive morphological operation for high-performance weather image processing," *IEIE Transactions on Smart Processing and Computing*, vol. 7, no. 6, pp. 424–432, 2018.

[6] R. Firoz, M. S. Ali, M. N. U. Khan, M. K. Hossain, M. K. Islam, and M. Shahinuzzaman, "Medical Image Enhancement Using Morphological Transformation," *Journal of Data Analysis and Information Processing*, vol. 04, no. 01, pp. 1–12, 2016.

[7] T. K. Dash, H. Driessen, O. A. Krasnov, and A. Yarovoy, "Precipitation Doppler Spectrum Reconstruction with Gaussian Process Prior," *2023 IEEE Conference on Antenna Measurements and Applications (CAMA)*, pp. 909–914, 2023.

[8] T. Dash, H. Driessen, O. Krasnov, and A. Yarovoy, "Doppler Spectrum Parameter Estimation for Weather Radar Echoes Using a Parametric Semi-analytical Model," *IEEE Transactions on Geoscience and Remote Sensing*, vol. 62, pp. 1–18, 2024.

[9] H. M. Finn, "Adaptive detection mode with threshold control as a function of spatially sampled clutter level estimates," *RCA Rev*, vol. 29, p. 414–464, 1968. [Online]. Available: https://api.semanticscholar.org/CorpusID:208092087

[10] J. C. Goswami and A. K. Chan, *Fundamentals of Wavelets: Theory, Algorithms, and Applications*. John Wiley and Sons, Inc., 2010.

[11] W. Lu, "User-centric signal processing of high-resolution meteorological phased array radar," Delft University of Technology, Tech. Rep., 2023. [Online]. Available: http://resolver.tudelft.nl/uuid:7fbb554c-1aa3-4d16-8f13-a16c988f5ff9

[12] A. Rényi, "On measures of entropy and information," in *Proceedings of the fourth Berkeley Symposium on Mathematics, Statistics and Probability*, 1961, pp. 547–561.

[13] M. El-Sayed and M. Ahmed, "Using renyi's entropy for edge detection in level images." *International Journal of Intelligent Computing and Information Sciences*, vol. 11, pp. 1–11, 2011.

[14] D. Sirmans and B. Bumgarner, "Numerical Comparison of Five Mean Frequency Estimators," *Journal of Applied Meteorology*, vol. 14, no. 6, pp. 991–1003, 9 1975.

[15] P. R. Mahapatra and D. S. Zrnić, "Practical Algorithms for Mean Velocity Estimation in Pulse Doppler Weather Radars Using a Small Number of Samples," *IEEE Transactions on Geoscience and Remote Sensing*, vol. GE-21, no. 4, pp. 491–501, 1983.

[16] T. Dash, A. Gîrdianu, O. A. Krasnov, and A. G. Yarovoy, "Beamforming for a Fast Scanning Phased Array Weather Radar," in *Proceedings of the 20th European Radar Conference*, 2023, pp. 290–293.